Contents lists available at ScienceDirect

Construction and Building Materials

journal homepage: www.elsevier.com/locate/conbuildmat





Carbonation resistance of alkali-activated GGBFS/calcined clay concrete under natural and accelerated conditions

Luís U.D. Tambara Jr. ^a, Astrid Hirsch ^b, Frank Dehn ^b, Gregor J.G. Gluth ^{a,*}

- a Division 7.4 Technology of Construction Materials. Bundesanstalt für Materialforschung und -prüfung (BAM). Unter den Eichen 87. Berlin 12205. Germany
- b Institute for Concrete Structures and Building Materials (IMB/MPA/CMM), Karlsruhe Institute of Technology (KIT), Gotthard-Franz-Str. 3, Karlsruhe 76131, Germany

ARTICLE INFO

Keywords:
Carbonation
Microstructure
Alkali-activated materials
Calcined clay
Ground granulated blast furnace slag

ABSTRACT

The carbonation resistance of alkali-activated materials (AAMs) is a crucial parameter for their applicability in concrete construction, yet the parameters influencing it are insufficiently understood to date. In the present study, the carbonation resistance of alkali-activated concretes with varying fractions of ground granulated blast furnace slag (GGBFS) and calcined clay (i.e., high, intermediate, and low Ca contents) were assessed under natural and accelerated conditions. Corresponding hardened AAM pastes were studied using X-ray diffraction, thermogravimetry, Raman microscopy, and mercury intrusion porosimetry. The carbonation resistance of the concretes at natural CO₂ concentration depended principally on their water/(CaO + MgO_{eq} + Na₂O_{eq} + K₂O_{eq}) ratio. The remaining variability for similar ratios was caused by difference the pore structures of the AAMs. For concrete with favorable water/(CaO + MgO_{eq} + Na₂O_{eq} + K₂O_{eq}) ratio and pore structure, the carbonation resistance was comparable to that of Portland cement concrete. The relationship between carbonation coefficients obtained under accelerated and natural conditions differed for concretes with high and low fractions of calcined clay, indicating that accelerated carbonation testing is less suitable to study the carbonation of low-Ca AAMs.

1. Introduction

Alkali-activated materials (AAMs) have been extensively studied as a possible route to significantly lowering the $\rm CO_2$ emissions related to cement production and use [1,2]. In addition, AAMs possess certain engineering properties, such as high acid resistance [3], which can make them highly valuable materials in special applications. However, uncertainties remain with regard to which parameters determine the carbonation resistance of these materials; clarification of these questions is required to enable a reliable use of them for reinforced concrete elements.

The carbonation process in ordinary Portland cement (OPC)-based concretes is a well-known phenomenon. Gaseous CO_2 present in the atmosphere penetrates the interconnected pores of the material and dissolves in the pore solution, forming carbonic acid ($\mathrm{H}_2\mathrm{CO}_3$). This acid initially reacts with portlandite [$\mathrm{Ca}(\mathrm{OH})_2$], one of the main products of Portland cement hydration, precipitating $\mathrm{Ca}(\mathrm{CO}_3)$ and water. The formation of this carbonate can result in the reduction of concrete porosity and permeability. When all or most of the portlandite is consumed, further carbonation leads to a decrease of the pH of the pore solution,

which creates an environment that facilitates corrosion of steel reinforcement in the concrete. The parameters that determine the carbonation rate of Portland cement-based concretes are well-understood, and established test methods exist.

Dissolution of CO2 in the pore solution of AAMs will also lead to a decrease of the pH, but, due to the fact that their portlandite content is generally lower and their pore solution is usually dominated by Na⁺, precipitation of CaCO₃ is not of major importance, while the decrease of pH may not be as pronounced as for conventional cements [4.5]. The latter is related to the differences between the pore solutions of AAMs and conventional cements and the consequently different carbonation products. Thermodynamic considerations about the Na₂O-CO₂-H₂O system [4] indicate the formation of natron (Na₂CO₃·10 H₂O) in AAMs at natural CO₂ concentration (0.04 %), trona [Na₃(CO₃)(HCO₃)·2 H₂O] formation at slightly higher CO2 concentrations, and formation of nahcolite (NaHCO₃) at CO₂ concentrations above 0.2 %; thermonatrite (Na₂CO₃·H₂O) is predicted only at temperatures above ~50 °C. However, the influence of additional components must be considered, as the presence of reactive aluminosilicates, serving as an additional alumina source, can suppress trona formation due to the influence of dissolved

E-mail address: gregor.gluth@bam.de (G.J.G. Gluth).

^{*} Corresponding author.

alumina. This effect enhances the formation of aluminosilicate gels, reducing alkali availability for carbonate formation [6]. Nevertheless, the rate of ingress of CO_2 and the associated decrease of pH (i.e., the carbonation rate of AAMs) are important parameters which must be minimized to avoid the risk of reinforcement corrosion in such materials.

Previous studies on the carbonation of AAMs have focused on high-Ca AAMs, *i.e.*, mainly alkali-activated ground granulated blast furnace slag (GGBFS). In these materials, carbonation immediately affects the C-A-S-H gel, the major reaction product, as there is no formation of portlandite in these systems. The decalcification of C-A-S-H can result in a loss of cohesion of the matrix and increases porosity, consequently reducing the mechanical strength and accelerating the carbonation process [7]. For natural carbonation of waterglass-activated slag, it has been observed that there is a predominant formation of vaterite and some aragonite, rather than calcite, in addition to the formation of natron. On the other hand, for slag activated with NaOH, a lower proportion of vaterite compared to aragonite was observed. Carbonation of these materials was reported to increase the matrix density, similar to what occurs in Portland cement, with a similar precipitation of crystals in the pores [8].

For AAMs based on blends of GGBFS and metakaolin, Bernal *et al.* [6] observed that addition of metakaolin significantly increased the carbonation rate under accelerated conditions, possibly due to a higher permeability of the samples. For carbonation in 3 % $\rm CO_2$ for 14 and 24 days, only the formation of calcite among the calcium carbonates was identified. Additionally, the authors observed the formation of trona and natron in samples containing only GGBFS, due to the carbonation of Na⁺ present in the pore solution [6]. Recently, the carbonation behavior of alkali-activated GGBFS/calcined clay blends spanning a wider compositional range (40–100 % calcined clay) has been studied [9]. In line with what was indicated by the previous data for GGBFS/metakaolin blends, the study showed an increasing carbonation rate with increasing fraction of calcined clay in the mixes.

While the above-mentioned works and many other studies have mainly investigated the carbonation behavior of high- and intermediate-Ca AAMs, meaningful data relating to the carbonation of low-Ca AAMs (generally alkali-activated fly ash or metakaolin) are scarce [13]. Nevertheless, a recent review which evaluated compositional and carbonation data for more than 150 AAMs [13], showed that the carbonation rate in low-Ca AAMs is generally higher than in high-Ca AAMs, and that the ratio water/(CaO + MgO_{eq} + Na_2O_{eq} + K_2O_{eq}) of the binder paste is useful to obtain an estimate of the carbonation rate of AAMs of widely varying compositions. However, significant scatter was observed for the relationship between carbonation rate and this ratio, indicating that additional factors play a major role for carbonation resistance, which are, however, currently only poorly understood.

In addition to uncertainties regarding the factors affecting the carbonation resistance of AAMs, open questions exist about the influence of the $\rm CO_2$ concentration on their carbonation behavior [4,5] and, thus, the significance of accelerated carbonation testing (i.e., testing at higher-than-natural $\rm CO_2$ concentrations) of these materials. An interlaboratory testing program [12] and a subsequent review [13] indicated that accelerated carbonation testing of low-Ca AAMs and conversion of the obtained results with the square-root-of-time law yields considerably lower carbonation rates than testing at natural $\rm CO_2$ concentration. However, the underlying reasons are poorly understood [13], and the amount of available data is possibly too low to regard the conclusion as

definite; thus, additional data is required to elucidate the issue.

To contribute to a better understanding of the factors that influence the carbonation behavior of AAMs over their full compositional range (Ca content), the present study involved determination of the carbonation rate under natural CO2 concentration and under accelerated conditions (1 % and 4 % CO₂) of concretes based on alkali-activated GGBFS/ calcined clay blends with respective fractions of 0-100 %, and determination of the phase assemblage and pore structure of corresponding pastes, before and after carbonation. The calcined clay corresponded to materials produced from what is generally referred to as low-grade kaolinitic clay, i.e., it is representative of the types of clay that are abundantly available in many parts of the world. The results of the study show that previous experience obtained for GGBFS-, fly ash-, and metakaolin-based AAMs can, in large part, be applied to GGBFS/ calcined clay-based AAMs. In addition, an important influence of the pore structure was found for the present starting materials, which led to variations of the carbonation rate despite comparable chemical compositions in some cases, and which points to possible routes to optimize the properties of AAMs.

2. Materials and methods

2.1. Starting materials

Calcined clay (CC) and ground granulated blast furnace slag (GGBFS) were used as the solid starting materials for the alkali-activated binders. The raw clay from which the CC was produced contains 55–56 % kaolinite, approx. 1 % illite, and mainly quartz and anatase as accessory minerals (see [14,15]; clay named K1 in the previous studies) and, thus, can be classified as low-grade kaolinitic clay. Calcination of the clay was conducted in a batch furnace, with the core temperature of the clay in the range of 720–740 $^{\circ}$ C for two hours. An ordinary Portland cement (OPC) CEM I 42.5 R according to EN 197–1 was used to produce reference materials. The chemical compositions of the solid binder starting materials, determined by inductively coupled plasma optic emission spectroscopy (ICP-OES) after total microwave digestion, are presented in Table 1.

Fig. 1 shows the XRD patterns of solid binder starting materials (for measurement conditions, see Section 2.3.2). The CC contained dehydroxylated illite/muscovite (PDFs #015–0603, #084–1306; cf. [14]), quartz (PDF #085–0335) and anatase (PDF #086–1156); the amorphous metakaolin causes the broad hump around 22° 2θ in the diffractogram. The diffractogram of the GGBFS exhibited an 'amorphous halo' between 20° and 38° 2θ . CEM I contained the typical phases of Portland cement: alite (3CaO \bullet SiO₂; PDF #042–0551), belite (2CaO \bullet SiO₂; hexagonal: PDF #023–1045, monoclinic: PDF #070–0388), aluminate (3CaO \bullet Al₂O₃; PDF #008–0005), ferrite (\sim 4CaO \bullet Al₂O₃ \bullet Fe₂O₃; PDF #011–0124) and anhydrite (CaSO₄; PDF #003–0377); gypsum (CaSO₄ \bullet 2 H₂O) was not observed.

The apparent densities, determined by helium pycnometry according to DIN 66137–2, of CC, GGBFS and CEM I were 2.62 g/cm³, 2.87 g/cm³ and 3.06 g/cm³, respectively. The particle size distributions of the CC and the GGBFS, determined by laser granulometry with a measuring range of 0.1 μ m to 900.0 μ m, are shown in the Supplementary Material, Fig. S1. The median particle size (d_{50}) of the CC was 28.9 μ m; the median particle size of the GGBFS was 10.8 μ m. The CC showed a tendency to agglomerate; its measured d_{90} was 169.2 μ m.

Alkaline solutions for alkali-activation were prepared from sodium silicate solution (30.2 % SiO₂, 14.7 % Na₂O, and 55.1 % H₂O), sodium hydroxide solution (18 M NaOH), and extra tap water.

Natural round-shaped silica aggregate with a nominal maximum grain size of 16 mm was used for the production of the concrete specimens. The grading curve of the aggregate was adjusted to lie between curves A 16 and B 16, specified in German standard DIN 1045–2 (Fig. S2).

⁵ The material that was blended with GGBFS was referred to as 'calcined clay' and classified as 'low-grade' in the study. The kaolinite fraction of the raw clay from which the material was obtained by flash calcination was reported to be 55 %, and XRD showed the calcined clay to contain almost only quartz as accessory mineral [9]. A material with the same origin and essentially identical composition was referred to as 'metakaolin' in previous studies [10–12].

 Table 1

 Chemical compositions of the binder starting materials.

	${ m SiO_2}$	Al_2O_3	Fe_2O_3	TiO_2	CaO	MgO	Na ₂ O	K_2O	SO_3	P_2O_5	Mn_2O_3	Other	LoI ^a
CC	60.1	28.3	2.8	3.4	0.8	0.9	0.2	1.7	0.1	0.1	-	1.6	2.0
GGBFS	33.6	12.4	0.3	1.1	39.1	8.0	0.4	0.7	1.1	-	0.3	3.0	n/a
CEM I	20.6	4.5	2.7	0.2	64.6	2.0	0.3	1.1	3.8	-	-	0.2	3.1

^a LoI: Loss on ignition, determined according to EN 196-2 at 1000 °C.

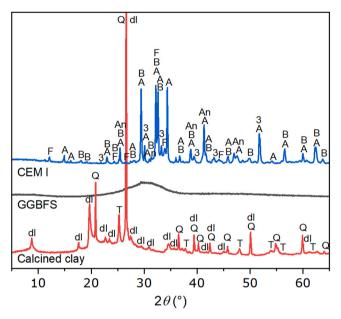


Fig. 1. XRD patterns of the solid binder starting materials. Major reflections are labelled 3: aluminate (C_3A) ; A: alite; An: anhydrite; B: belite; dI: dehydroxylated illite/muscovite; F: ferrite (C_4AF) ; Q: quartz; T: anatase.

2.2. Mix designs and specimen production

Six alkali-activated concrete mixes were produced with systematically varied fractions of CC and GGBFS, with CaO contents of the binder from $\sim\!0$ % (CC only) to $\sim\!40$ % (GGBFS only). The nomenclature of the concretes and pastes, applied in what follows, is based on the percentages of CC and GGBFS in the binders, with the number following C indicating the fraction of CC and the number following S indicating the fraction of GGBFS. For example, 'C100' denotes a concrete or paste made from CC as the only solid binder starting material, and 'C40S60' denoting a blend of 40 % CC and 60 % GGBFS as the solid binder components.

Initial attempts to produce the concrete mixes with identical paste volumes and activator moduli, and systematically varied activator concentration failed, leading partly to mixes with very poor workability and partly insufficient 28-day compressive strength. Therefore, the mix designs were individually optimized to achieve sufficient workability and compressive strength. The optimization led to the final mix designs shown in Table 2, which were used for the subsequent experiments.

In addition to alkali-activated concretes, an OPC concrete (denoted 'CEM I' in what follows) was produced as a reference. The CEM I concrete was produced with a water/cement ratio (w/c) of 0.45 and a cement content of 400 kg/m³. The measured air content of the fresh concrete was 1.9 %, and the density was 2.36 g/cm³; the 28-day compressive strength of the concrete was 68.3 MPa.

Concrete mixing was conducted in the following sequence: One minute of dry mixing of aggregate and solid binder starting materials, 30 s mixing during which sodium silicate solution, sodium hydroxide solution, and extra water were continuously added, and subsequently further mixing for 3.5 minutes (*i.e.*, to a total mixing time of 5 minutes).

Table 2Alkali-activated concrete mix designs, activator solution and mix design parameters, measured fresh concrete properties, and 28-day compressive strengths.

Mix designs:						
Material	C100	C80S20	C60S40	C40S60	C20S80	S100
CC (calcined	388.1	340.0	277.7	176.0	84.0	-
clay) (kg/m ³)						
GGBFS (kg/m ³)	-	85.0	185.0	264.0	336.0	400.0
Sodium silicate	292.7	188.9	108.9	177.1	61.2	42.0
sln. (kg/m³)						
18 M NaOH sln.	59.6	38.3	46.7	42.2	26.2	18.0
(kg/m^3)						
Extra water	49.7	118.2	138.4	77.5	131.0	140.0
(kg/m^3)						
Aggregate (kg/ m ³)	1474	1479	1519	1603	1715	1765
Activator						
parameters:						
$(Na_2O + SiO_2)$	38.2 %	20.7 %	22.6 %	38.9 %	29.9 %	12.8 %
fraction in						
activator sln.						
Silica modulus	1.40	1.40	1.02	1.32	1.02	1.02
(SiO ₂ /Na ₂ O)						
(mol/mol)						
Concrete mix						
design						
parameters:						
Liquid/solid	1.04	0.81	0.64	0.67	0.52	0.50
ratio of paste ^a						
(kg/kg)	0.46	0.55	0.40	0.00	0.00	0.41
Water/binder	0.46	0.55	0.43	0.33	0.32	0.41
ratio of paste ^b						
(kg/kg)	0.160	0.070	0.072	0.110	0.070	0.022
Na ₂ O/solid	0.169	0.079	0.073	0.110	0.078	0.032
ratio of paste ^c (kg/kg)						
Total paste in	790.1	770.4	756.7	736.8	638.4	600.0
concrete (kg/	790.1	770.4	/30./	/30.6	030.4	000.0
m ³)						
Fresh concrete						
properties:						
Air content (vol	6.0	2.7	2.2	2.5	2.0	2.0
%)	0.0	2.,		2.0	2.0	2.0
Bulk density (g/	2.24	2.27	2.31	2.31	2.36	2.37
cm ³)						
Hardened						
concrete						
mechanical						
strength:						
28-day	24.1	31.1	42.1	70.6	60.7	65.5
compressive						
strength						
(MPa)						

 $^{^{\}rm a}$ 'Liquid' represents the complete activator solution, including dissolved solids (Na $_{\rm 2}O+SiO_{\rm 2})$; 'solid' represents only the solid binder starting materials (CC and/or GGBFS).

 $^{^{\}rm b}$ 'Water' represents the water contained in the activator solution; 'binder' represents the sum of the solids dissolved in the activator solution (Na₂O + SiO₂) and the solid binder starting materials (CC and/or GGBS).

^c 'Na₂O' represents only Na₂O dissolved in the activator solution; 'solid' represents only the solid binder starting materials (GGBFS and/or CC).

After mixing, a fraction of the fresh concrete was used for determining flow diameter EN 12350–5 and air content according to EN 12350–7, and the remainder was cast into cubic molds with an edge-length of 150 mm and prismatic molds with dimensions 100 mm \times 100 mm \times 400 mm. The casting was done in two layers, vibrating each layer for 20 s. The molds were covered with polythene (PE) sheets, and after 24 hours, the specimens were stripped from the molds and stored in closed plastic bags in the climate chamber at (23 \pm 2) $^{\circ}$ C for 27 days. After the total curing time of 28 days, the concrete cubes were used for compressive strength testing according to EN 12390–3. The flow diameters of the fresh concrete mixes and their compressive strengths after 28 days of curing are shown in Figs. S3 and S4, together with some of their compositional parameters.

Concurrently with the production of the concrete specimens, cubic paste specimens with an edge-length of 20 mm were produced, with the paste compositions being identical to those of the corresponding concrete mixes. Mixing of the pastes was done in a planetary centrifugal mixer (Thinky Mixer ARE-500) operating at a speed of 1250 rpm for a total of 4 minutes. The paste specimens were subjected to the same curing conditions as the concretes.

2.3. Methods

2.3.1. Carbonation resistance testing

For the natural and accelerated carbonation tests, prismatic concrete specimens measuring $100 \text{ mm} \times 100 \text{ mm} \times 400 \text{ mm}$ were used. After the curing period of 28 days (Section 2.2), the specimens were split into halves, and the carbonation depths were measured (time t_0) by spraying a phenolphthalein indicator solution on the fracture surfaces (see below). For all concrete mixes, the carbonation depths were 0 mm in this initial measurement. Subsequently, the specimens were transferred into the respective environments for carbonation testing.

Natural carbonation testing was conducted as described in EN 12390–10. The exposure conditions were CO_2 concentration: 0.04 %, temperature: (20 ± 5) °C, and relative humidity (RH): 65 %. Carbonation depth measurements were performed after 50, 100, and 200 days of exposure.

For accelerated carbonation test, the specimens were transferred after curing to carbonation chambers with RH =60~% and a temperature of (20 \pm 5) °C. Testing was done at two different CO $_2$ concentrations, 1 % and 4 %. Determination of the carbonation depths were carried out after 1, 7, 35, and 91 days of exposure.

All carbonation depth measurements were performed by spraying a $1\,\%$ phenolphthalein indicator solution in $70\,\%$ ethanol and $30\,\%$ deionized water by volume onto freshly broken surfaces, maintaining a minimum distance of 5 cm from the original surfaces of the prismatic specimens. Three equally spaced points were measured for each edge of a created surface, totaling $12\,$ measurements for each of the surfaces. The average depth of carbonation was calculated for the two surfaces as the arithmetic mean of the $24\,$ individual values.

For the alkali-activated concrete mixes, carbonation depths were determined immediately after fracturing the specimens, as the surface color after spraying the indicator solution changed quickly. Mixes with lower CaO contents exhibited a color change in the areas that were initially colorless (i.e., carbonated), turning light pink in less than 5 minutes after spraying, making it difficult to read the carbonation depths at later times (cf. [12]). For the CEM I concrete, measurements were taken 15 minutes after spraying the indicator solution.

Concurrently with the exposure of concrete specimens, cubic paste specimens cured for 28 days (Section 2.2) were exposed to the same carbonation conditions.

2.3.2. X-ray diffraction, thermogravimetry and Raman microscopy

For X-ray diffraction (XRD) analyses and thermogravimetric analyses (TGA), fragments of the pastes after curing (Section 2.2) and after carbonation were obtained by fracturing paste specimens in a

compressive strength testing device. Hydration was stopped by submerging the fragments in isopropanol. The isopropanol was exchanged after 3 hours, 1 day, and 3 days. After a total of 7 days of immersion, the samples were dried in an oven at 40 $^{\circ}$ C for 24 hours. The dried samples were manually ground with mortar and pestle (agate) to a fine powder, which was used for phase assemblage determination (XRD and TGA).

XRD measurements were conducted on a BRUKER D2 Phaser (2nd Gen) instrument using Cu-K α radiation ($\lambda=1.5419$ Å) at 30 kV and 10 mA. The primary Soller slit was set to 2.5°, and the divergence slit to 1.0 mm (equivalent to 0.95°). The detector was the LYNXEYE XE-T detector with 2.5° secondary Soller slits. The step size was 0.02° 2θ with a measurement time per step of 1 s; the scanning range extended from 5° to 65° 2θ . The sample holders for the XRD measurements were filled by back loading. Samples were spun at 15 rpm during the measurements to improve particle statistics.

TGA was performed with a Mettler Toledo device with a sensitivity of 0.1 μ g, operated at temperatures ramped from 40 to 1000 °C at a rate of 10 °C/min under flowing nitrogen gas (80 ml/min). Sample masses for TGA measurements were approx. 10 mg.

The samples for confocal Raman microscopy (CRM) measurements were cubic paste specimens after curing and carbonation. Measurements were first taken at their outer surfaces; subsequently, the cubes were cut into halves and the obtained cross-sections analyzed. The measurements were performed using a WITec Alpha 300 R Raman microscope, equipped with a 532-nm excitation laser, a spectrometer UHTS-300-VIS (grating with 600 grooves/mm) and a thermoelectrically cooled CCD camera Andor DV-401A-BV-532 at $-62\,^{\circ}\text{C}$. Spectra were recorded with a laser power of 18 mW and an integration time of 50 ms, spanning a wavelength range from 0 to 2100 cm $^{-1}$. Mappings were done for selected areas with dimensions of $70~\mu\text{m} \times 70~\mu\text{m}$, and a theoretical pixel resolution of $\sim\!0.30~\mu\text{m}$. The software used to process the spectra, identify characteristic bands, and create phase maps was WITec Project 6.1.

2.3.3. Mercury intrusion porosimetry

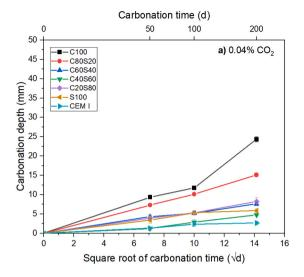
Pore structure analyses of 28-day cured pastes, after 200 days of exposure to natural carbonation, and after 91 days of exposure at $1\,\%$ or $4\,\%$ CO₂, were done by mercury intrusion porosimetry (MIP) using a MicroActive AutoPore V 9600. Fragments of pastes after stopping hydration (Section 2.3.2) were evaluated. The maximum applied pressure was 420.5 MPa, and for the calculation of pore sizes a surface tension of 485 mN/m, a contact angle of 141.3° , and cylindrical pores were assumed

From the resultant apparent pore size distributions, the cumulative porosities and the threshold radii $(r_{\rm thr})$ [16,17] were determined. The threshold radius provides insight into the pore size at which percolation through the analyzed porous solid occurs, a crucial factor for understanding permeability and diffusion in the studied materials [16]. The threshold radius was determined by the graphical method, *i.e.*, by drawing tangents on the steep and the flat part of the cumulative pore size distribution curve and taking the radius at their intersection as $r_{\rm thr}$. If two distinct steps were identified in the cumulative distribution curve, the step at the lower pore size was chosen for determination of $r_{\rm thr}$, as this is the pore size associated with complete penetration of the sample.

3. Results

3.1. Carbonation depth

Fig. 2 shows the carbonation depths of the concretes over time under natural and accelerated carbonation conditions. For natural conditions, the concrete mixes can be assigned to three performance levels. C100 and C80S20 exhibited high carbonation rates with carbonation depths of ~25 mm for C100 and ~15 mm for C80S20 after 200 days. C60S40, C20S80 and S100 exhibited moderate carbonation depths ranging from 3.5 to 4.3 mm after 50 days, and in the range of approx. 6–8 mm after



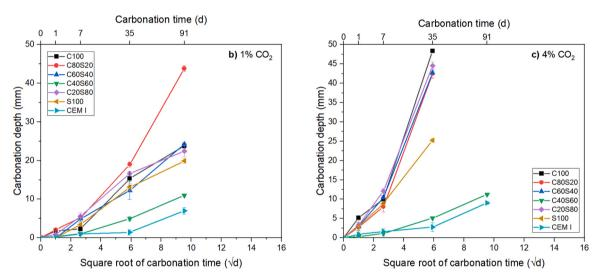


Fig. 2. Depths of carbonation of the concretes at a) natural CO₂ concentration, and under accelerated conditions: b) 1 % CO₂, and c) 4 % CO₂.

200 days. The lowest carbonation rates were found for C40S60 and CEM I; their carbonation depths were $\sim\!1.2$ mm after 50 days, and $\sim\!2.5$ mm after 100 days, while they were 4.7 mm for C40S60 and 2.7 mm for CEM I after 200 days.

Under accelerated conditions, *i.e.*, 1 % and 4 % $\rm CO_2$, the carbonation rates of the two best-performing mixes, C40S60 and CEM I, were considerably lower than those of the other concretes. The carbonation depths of the latter concretes with inferior-performance were similar to each other at most carbonation times, with two notable exceptions: the carbonation depth of C80S20 was higher than those of the other concretes after 35 days at 1 % $\rm CO_2$, and the carbonation depth of S100 was lower than those of C100, C80S20, C60S40 and C20S80 after 35 days at 4 % $\rm CO_2$. After 91 days of carbonation in an atmosphere with 4 % $\rm CO_2$, all concrete specimens (cross sectional area: 100 mm \times 100 mm) except C40S60 and CEM I were fully carbonated.

3.2. Phase assemblage

The XRD patterns of the hydrated pastes after 28-day curing, and after carbonation at natural CO₂ concentration as well as under accelerated conditions are shown in Fig. 3. After curing, the diffractogram of S100 exhibited a broad hump in the range approx. $25^{\circ}-35^{\circ}~2\theta$ and a peak at $29.5^{\circ}~2\theta$, indicative of C-(N-)A-S-H gel, as well as reflections of a hydrotalcite-like phase. In the diffractograms of the alkali-activated

GGBFS/CC blends, a broad hump in the range approx. $20^{\circ}-35^{\circ}$ 2θ , indicating the presence of a mix of N-A-S-H and C-(N-)A-S-H gels, or only N-A-S-H gel in the materials with high CC fraction, was present. For these blends, the peaks of the crystalline impurities observed also for the anhydrous CC were found, viz., quartz, dehydroxylated illite/muscovite, and anatase. A higher intensity of these peaks was observed with increasing fraction of CC in the materials, as expected. The diffractograms of C20S80 and C40S60 exhibited minor peaks assigned to sodium silicate (Na₂O•2SiO₂; PDF #018-1241); this is likely related to the comparatively high concentrations of Na2O and SiO2 in the activator solutions and the low water/binder ratios of these pastes, which may have led to the incomplete reaction of Na2O and SiO2 to form binder gels. Low-intensity peaks of thermonatrite, formed through slight carbonation during curing (and subsequent drying), were observed for C100. For CEM I, the formation of the typical OPC hydration products was observed, with the presence of portlandite and ettringite as the main crystalline phases, along with AFm phases (hemicarbonate and monocarbonate), indicated by a broad reflection in the range 10° – 12° 2θ . The main binder phase in hydrated OPC, C-S-H gel, can usually not be identified in XRD patterns, due to its poor crystallinity.

After carbonation, the three crystalline polymorphs of $CaCO_3$ – calcite, vaterite, aragonite – were observed in all alkali-activated pastes containing GGBFS, their relative abundance varying with paste mix design and CO_2 concentration during testing (Fig. 3, Fig. S5). The alkali-

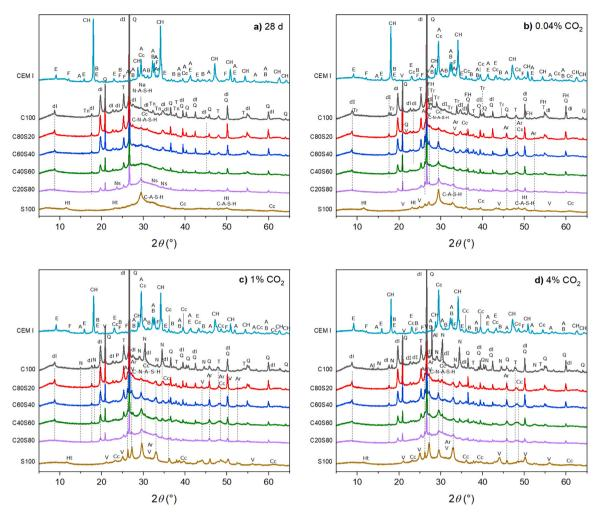


Fig. 3. XRD patterns of the pastes after a) 28 days of curing, b) 200 days of carbonation at natural CO_2 concentration, c) 91 days of carbonation at 1 % CO_2 , and d) 91 days of carbonation at 4 % CO_2 . Major reflections are labelled A: alite; Ar: aragonite; B: belite; Cc: calcite; CH: portlandite; dI: dehydroxylated illite/muscovite; E: ettringite; F: ferrite (C_4 AF); FH: ferrous hydroxide; Ht: hydrotalcite-like phase; N: nahcolite; Na: natrite; Ns: sodium silicate (Na_2O_2 SiO₂); Q: quartz; T: anatase; Tn: thermonatrite; Tr: Trona.

activated GGBFS/CC blends contained also small amounts of nahcolite after accelerated carbonation (1 % and 4 % $\rm CO_2$). The diffractograms of C100 exhibited peaks of nahcolite, trona and/or natrite (Na₂CO₃), depending on the $\rm CO_2$ concentration. The dominating carbonate in CEM I after carbonation at all $\rm CO_2$ concentrations was calcite, as expected; however, reflections of vaterite were also found for all carbonation conditions.

The relative abundance of carbonates and other phases in the individual pastes after carbonation partly differed depending on the CO₂ concentration during carbonation, particularly for S100 and C100 (Fig. 3, Fig. S5). For S100, the relative intensities of the vaterite and aragonite reflections tended to increase with increasing CO2 concentration. There was also an apparent decrease of the intensity of the main peak of the hydrotalcite-like phase with increasing CO2 concentration, possibly related to its transformation during uptake of CO₂ [18,19]. For C100, trona was the only sodium carbonate after carbonation at natural CO₂ concentration. After carbonation of that paste at 1 % and 4 % CO₂, high-intensity peaks of nahcolite and natrite (presumably formed by dehydration of nahcolite [20] during drying) were present, while reflections of trona were absent. These results are in general agreement with the dependence of the stability of sodium carbonate phases on CO₂ concentration; namely, natron and/or trona are expected at CO2 concentrations at or slightly above natural levels, while nahcolite is the stable phase at CO_2 concentrations above $\sim 0.2 \%$ [4]. Minor peaks of ferrous hydroxide [Fe(OH)₂] (PDF #026–0792) were identified for C100 after carbonation at natural CO2 concentration.

Fig. 4 shows the derivative thermogravimetry (DTG) curves of the pastes. The TGA curves are shown in Fig. S6, and the weight losses for specific temperature ranges are provided in Table S1. The large, broad band, centered at around 100 °C in the DTG curves of all pastes is mainly attributed to their respective major reaction products, i.e., C-(N-)A-S-H and/or N-A-S-H for the alkali-activated pastes, and C-S-H and ettringite for CEM I. Bands at $\sim\!250$ °C and $\sim\!350$ °C in the DTG curve of S100 after 28-day curing are assigned to the hydrotalcite-like phase [21]. In the DTG curve of CEM I after curing, the band at approx. 350–500 °C is assigned to portlandite, and the broad band at approx. 500–750 °C with a peak at $\sim\!650$ °C to calcite; decomposition of the carbonate-containing AFm phases likely contributed to the latter broad band (shoulder/peak at $\sim\!600$ °C), and the bands at $\sim\!250$ °C and $\sim\!350$ °C [21].

Carbonation of the pastes caused the appearance of several new bands in their DTG curves in the range approx. 400–750 °C (Fig. 4, Fig. S6), related to several carbonates [21,22]. The main DTG signals of nahcolite and trona, detected by XRD in C100 and some of the blends with CC, are expected at around 90–180 °C [20] and, thus, overlap with the bands of the main hydration products of these pastes. The minor signals at ~850 °C in some of the DTG curves can be assigned to Na₂CO₃ [23], formed from other carbonates at lower temperatures during TGA [20].

For the alkali-activated pastes with a moderate to high GGBFS fraction, i.e., C40S60, C20S80, and S100, the relative intensity of the

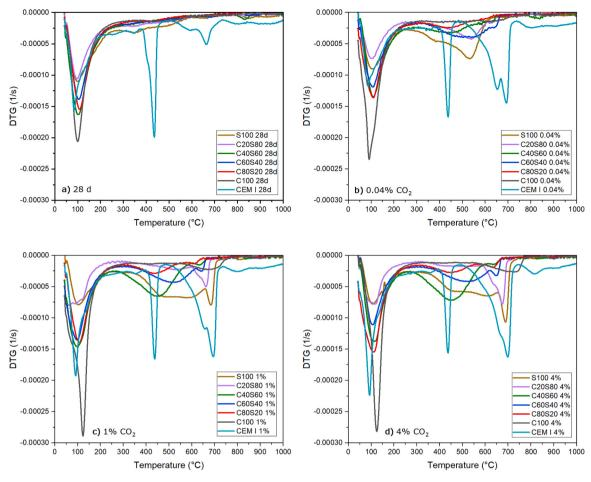


Fig. 4. DTG curves of the pastes after a) 28 days of curing, b) 200 days of carbonation at natural CO₂ concentration, c) 91 days of carbonation at 1 % CO₂, and d) 91 days of carbonation at 4 % CO₂.

DTG bands in the temperature range 250-750 °C differed between the carbonation conditions. C40S60 exhibited a broad band centered at ~450 °C, which was considerably more intense after accelerated carbonation (1 % and 4 % ${\rm CO_2}$) than after natural carbonation. C20S80 and S100 exhibited a band with a peak at slightly above 500 °C after natural carbonation, while after accelerated carbonation this band was smaller and a prominent peak at ~ 700 °C was present. For CEM I, a major asymmetric peak at ~700 °C was present for all carbonation conditions, which can be assigned to calcite, as identified by XRD. Based on this, the peaks at \sim 700 $^{\circ}$ C in the GGBFS-containing alkali-activated pastes too, particularly S100, C20S80 and C60S40, are assigned to calcite. The signals below 600 °C can be attributed to vaterite and aragonite (after recrystallization to calcite), and possibly amorphous CaCO₃, all of which decompose at significantly lower temperatures than calcite [21,22] If the hydrotalcite-like phase in S100 had taken up CO2 during carbonation, this could have led to its transformation and, thus, to a shift of its decomposition temperatures (DTG peaks). As some polytypes of hydrotalcite release CO2 only at temperatures only at ~450 °C [24], these may have contributed to the corresponding peaks in the DTG curves of S100.

The alkali-activated blends with a higher CC fraction, C80S20 and C60S40, exhibited similar DTG traces after all carbonation conditions, with a major broad peak centered around 500 °C, and a smaller peak at considerably higher temperatures. As with the GGBFS/CC blends with a higher fraction of GGBFS, these can be assigned to the different polymorphs of CaCO₃. However, it cannot be ruled out that the higher Na/Ca ratio of the pastes with higher CC fraction, *i.e.*, the higher relative abundance of Na in these systems, led to a shift of the decomposition

temperatures, which makes these assignments less certain.

For C100, a significant shift of the main DTG peak from \sim 100 °C to \sim 120 °C could be observed after accelerated carbonation (1 % and 4 % CO₂), which can be attributed to the presence of nahcolite and trona [20] in addition to the N-A-S-H gel. The smaller peaks at \sim 700 °C, which are particularly prominent after accelerated carbonation, are not due to calcite; it is likely that these are caused by the thermal dissociation of natrite, whose decomposition temperature can be lowered by the presence of CaO in the system [23], and thus possibly also by other species.

3.3. Raman microscopy

Representative Raman spectra of the carbonated pastes, obtained by averaging the spectra obtained for one 70 μm \times 70 μm area for each specimen, are shown in Fig. 5. Assignment of the bands in the Raman spectra and identification of major phases was aided by the RRUFF database [25]. For all pastes containing CC, anatase, which was present in the calcined clay, caused prominent bands at Raman shifts of 637 cm^{-1} , 513 cm^{-1} , 396 cm^{-1} , 205 cm^{-1} and 150 cm^{-1} , with the latter one exhibiting the highest intensity. Quartz, also present in the calcined clay, was identified through bands at $\sim 1085 \text{ cm}^{-1}$, \sim 800 cm⁻¹, 465 cm⁻¹, 400 cm⁻¹, 197 cm⁻¹ and 147 cm⁻¹. Identification of N-A-S-H gel in the alkali-activated pastes with a high CC fraction is difficult, due to the presumably low intensity of the Raman signals of this amorphous phase (cf. [26,27]). Paste CEM I and the pastes with GGBFS, but not paste C100, exhibited peaks at $\sim 1000 \text{ cm}^{-1}$ and \sim 900 cm⁻¹ (Fig. 5, magnified ranges 700–1100 cm⁻¹ on the right-hand side), which are assigned to symmetric stretching vibrations of Q² SiO₄

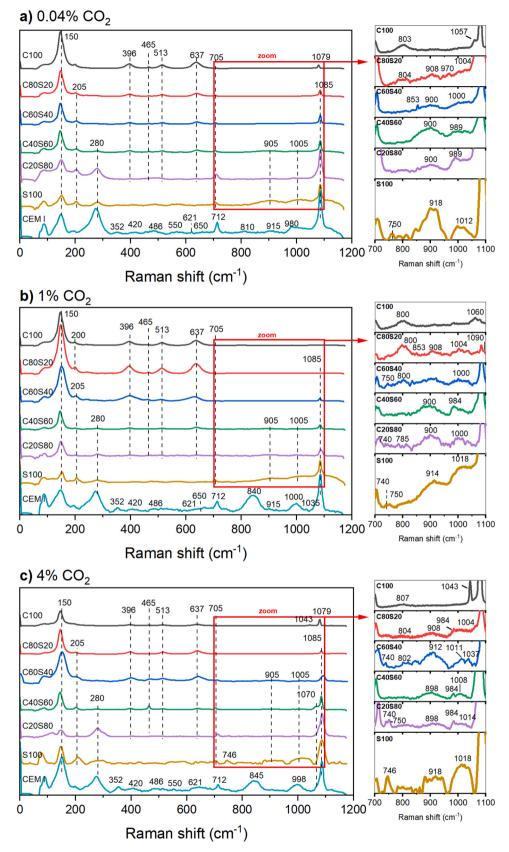


Fig. 5. Raman spectra of the pastes after a) 200 days of carbonation at natural CO_2 concentration, b) 91 days of carbonation at 1 % CO_2 , and c) 91 days of carbonation at 4 % CO_2 .

units and Q 1 SiO $_4$ units, respectively, in C-S-H for CEM I, and in C-(N-) A-S-H for the alkali-activated GGBFS/CC blends and S100 [28–30]. The bands centered at $\sim\!650~{\rm cm}^{-1}$ in the spectra of CEM I can likely be assigned to Si–O–Si bending in C-S-H [28,29]. Additional bands in the Raman spectra of CEM I can be assigned to portlandite (352 cm $^{-1}$), ettringite (352 cm $^{-1}$, $\sim\!550~{\rm cm}^{-1}$ and 621 cm $^{-1}$) and possibly AFm phases [Al(OH) $_6$ at $\sim\!530~{\rm cm}^{-1}$] [28].

Carbonates in the pastes were identified through their characteristic bands at Raman shifts of approx. 1040-1090 cm⁻¹ and at around 700 cm^{-1} (Figs. 5 and 6, Fig. S7). For the two CaCO₃ polymorphs calcite and aragonite, the major peak of the $v_1(CO_3^{2-})$ symmetric stretching is found at $1085\ \text{cm}^{-1}$, while the analogous vibration in vaterite causes a peak at 1090 cm⁻¹. The v_4 in-plane vibration is found at ~712 cm⁻¹ for calcite, at \sim 745 cm⁻¹ for vaterite, and at \sim 700 cm⁻¹ for aragonite [28, 31–34]. In addition, a signal of the v_2 or v_3 vibration of aragonite, often very minor, is detected at 853 cm⁻¹ [28,35]; it is noted that amorphous CaCO₃ may cause a signal at a similar Raman shift [28]. For paste C100, bands associated with sodium carbonates [36-39] were identified. Nahcolite exhibits a strong v_1 band at 1044 cm⁻¹, a signal at 684 cm⁻¹ and a weaker signal at \sim 640 cm⁻¹ The peak at 1062 cm⁻¹ represents the symmetric stretching mode of the carbonate group in trona; an additional band is found at 700 cm⁻¹ for this phase. It is noted that these shifts are similar to those of thermonatrite, which exhibits Raman signals in the range of $1067-1070 \text{ cm}^{-1}$ and at $\sim 700 \text{ cm}^{-1}$. Natrite can be identified by its peak at 1079 cm⁻¹, while it exhibits a band at $\sim 700 \text{ cm}^{-1} \text{ too.}$

Phase maps of the alkali-activated pastes after carbonation, generated using the above assignments of the Raman bands of the various carbonates (Fig. S7), are shown in Fig. 6. The phase maps of C100 are in line with the XRD results, in that only trona was identified after natural carbonation, while nahcolite and/or natrite (presumably formed by drying of nahcolite) were present after accelerated carbonation. For most of the alkali-activated pastes containing GGBFS, all three CaCO₃ polymorphs were observed for all $\rm CO_2$ concentrations, again generally in accordance with the phase assemblages determined by XRD and TGA. Notably, these polymorphs occurred next to each other on a length scale of a few micrometers in the phase maps; thus, a systematic sequence of prevalent $\rm CaCO_3$ polymorphs (e.g., with the relative amounts evolving from outer to inner regions) could not be identified.

3.4. Pore structure

Fig. 7 shows the mercury porosimetry curves of the pastes after 28 days of curing, and after natural and accelerated carbonation; the total porosities and threshold radii obtained by MIP are summarized in Table 3. The MIP curves grouped for each of the individual pastes are shown in Fig. S8.

For the as-cured pastes, the porosity results aligned generally well with the compressive strengths of the corresponding concretes (Table 2), with a lower MIP porosity mostly associated with a higher concrete strength. The threshold radii after 28-day curing differed considerably between the pastes, with the lowest $r_{\rm thr}$ determined for C40S60 and the second-lowest for S100. In addition, the total porosity of C40S60, determined by MIP, was the lowest of all pastes. This shows that the pore structure of C40S60 was particularly dense compared to the other pastes.

Carbonation led to slight changes of the MIP porosities and threshold radii of the alkali-activated pastes, generally (but not always) leading to an apparent slight coarsening of the pore structure. In addition, carbonation of C100 led to a significantly increased volume of pores with entries larger than $r_{\rm thr}$, which can possibly be attributed to a partial decomposition of binder gel in that paste [40]. Analogous increases were observed for C40S60 after natural carbonation, and for S100 after carbonation at 1 % and 4 % CO₂. However, since MIP results in the coarse-pore size range are influenced by microcracks and other defects, which might not be directly related to the pore structure as generated by

the hydration products, the significance of these findings is uncertain. For CEM I, natural carbonation induced only slight changes of MIP porosity and $r_{\rm thr}$, while carbonation at 1 % and 4 % CO₂ caused a considerable decrease of the porosity and the threshold radius, which is assigned to the precipitation of significant amounts of CaCO₃ (mostly calcite).

Finally, it is noted that the MIP measurements of paste C20S80 after carbonation (all three CO₂ concentrations) vielded uncommon cumulative pore entry size distributions with unrealistically high threshold radii on the order of $1-2 \mu m$ and very steep increases at this pore size (Fig. S8e). Since paste C20S80 had a very low viscosity in the fresh state, the unexpected MIP results are attributed to sedimentation in that paste during curing, which presumably led an incoherent microstructure and, thus, to disintegration of the specimens under the high pressures during MIP. The corresponding results do not reflect the microstructure of concrete C20S80: Due to the presence of aggregates, this concrete exhibited no signs of sedimentation (though its flow diameter was comparatively large, Fig. S3); thus, its microstructure and carbonation resistance were likely not significantly affected by segregation. It is further noted that the phase quantities in paste C20S80 appeared not to have been affected by sedimentation, indicated by the fact that the phase analyses for this paste aligned well with its chemical composition as compared to the other pastes.

4. Discussion

4.1. Influence of AAM composition on carbonation resistance

From the carbonation depth-*versus*-time data (Fig. 2), the coefficient of carbonation, k_c , can be obtained, assuming that the square-root-of-time law holds, by fitting a linear function through the carbonation depths plotted over the square root of time [41,42]. Since in the present study, the carbonation depths were 0 mm before exposure to carbonation conditions for all concretes, the functions were forced through the origin of coordinates in all cases; data points that represented fully carbonated specimens (as occurred at 4 % CO₂) were not considered for fitting. The resulting fits (including k_c and coefficients of determination, R^2) are shown in Fig. S9, and the resulting k_c are listed in Table 4.

Table 4 shows that there was a trend of increasing $k_{\rm C}$ with increasing ${\rm CO}_2$ concentration during carbonation, as expected, and that the $k_{\rm C}$ tended, with exceptions, to decrease with increasing GGBFS fraction in the binder of the alkali-activated concretes. Importantly, the coefficients of carbonation under natural carbonation conditions, $k_{\rm C-nat}$, were very similar for the CEM I concrete (0.21 mm/ \sqrt{d}) and the alkali-activated concrete C40S60 (0.29 mm/ \sqrt{d}). This demonstrates that well-designed and optimized alkali-activated concretes can achieve a carbonation resistance that is comparable to those of conventional (OPC-based) concretes.

The general decrease of the coefficients of carbonation of the alkaliactivated concretes with increasing GGBFS fraction might be explained with the concept that for OPC and blended cement concretes, carbonation coefficients generally decrease with decreasing $w/\text{CaO}_{\text{reactive}}$ ratio, where w is the water content and $\text{CaO}_{\text{reactive}}$ is the content of reactive CaO of a cement paste or concrete [12,43,44]. The applicability of the relationship can be rationalized by considering that w determines the porosity and, thus, the diffusion coefficient of CO_2 in a hydrated cement paste and that $\text{CaO}_{\text{reactive}}$ largely determines the amount of hydration products that are able to bind CO_2 and, thus, retard the progress of the carbonation front.

However, a recent data analysis [13] has shown that the w/CaO ratio (as a proxy for w/CaO_{reactive}) of AAMs is not useful to predict their carbonation resistance over their full compositional range, *i.e.*, including low-Ca AAMs. It was further shown that, instead, there is a considerably better correlation between k_{c-nat} of AAMs and their w/(CaO + MgO_{eq} + Na₂O_{eq} + K₂O_{eq}) ratio, where MgO_{eq}, Na₂O_{eq} and K₂O_{eq} are "equivalent" contents of MgO, Na₂O and K₂O, respectively, calculated by multiplying

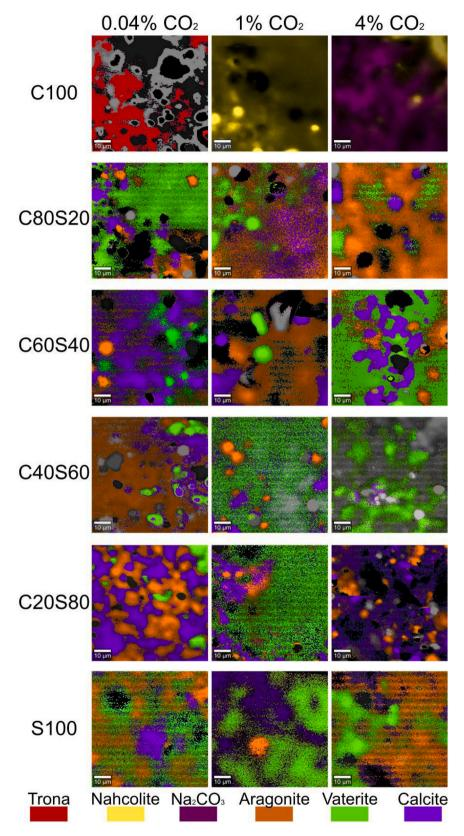


Fig. 6. Raman phase maps of the alkali-activated pastes after 200 days of carbonation at natural CO_2 concentration, 91 days of carbonation at 1 % CO_2 , and 91 days of carbonation at 4 % CO_2 .

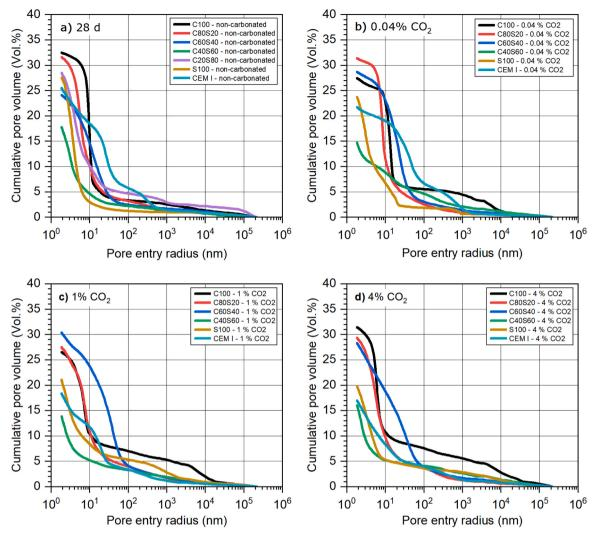


Fig. 7. Cumulative pore entry size distributions, determined by mercury intrusion porosimetry, of the pastes after a) 28 days of curing, b) 200 days of carbonation at natural CO₂ concentration, c) 91 days of carbonation at 1 % CO₂, and d) 91 days of carbonation at 4 % CO₂.

Table 3Results of the MIP analyses of the non-carbonated and the carbonated pastes.

Sample	28-day cured ^a		0.04 % CO ₂ ^a		1 % CO ₂ ^a		4 % CO ₂ ^a	
	ε (%)	r _{thr} (nm)	ε (%)	r _{thr} (nm)	ε (%)	r _{thr} (nm)	ε (%)	r _{thr} (nm)
C100	32.5	13.4	27.4	16.2	26.6	9.6	31.4	8.1
C80S20	31.6	9.3	31.4	12.9	27.5	12.2	29.3	10.7
C60S40	24.1	30.7	28.7	44.5	30.4	73.3	28.3	75.2
C40S60	17.2	5.6	14.7	$(4.4)^{b}$	13.8	3.6	16.0	3.9
C20S80	28.5	9.4	n/a	n/a	n/a	n/a	n/a	n/a
S100	27.6	5.7	23.7	$(22.9)^{b}$	21.1	6.4	19.8	7.2
CEM I	25.5	40.8	21.7	70.6	18.4	27.6	17.0	13.4

^a ε : total porosity; r_{thr} : threshold radius

their contents in the binder (including the activator) by the ratio of the molar mass of CaO to the molar mass of the respective oxides. The correlation was explained by the fact that these oxides are able to bind ${\rm CO_2}$ by forming carbonates, similar to CaO in the binder. This means that $w/({\rm CaO+MgO_{eq}+Na_2O_{eq}+K_2O_{eq}})$ can be used to obtain an approximate estimate of $k_{\rm c-nat}$ of AAMs, though the scatter of the data underlying the relationship was significant.

A plot of the $k_{\text{c-nat}}$ of the alkali-activated concretes of the present study versus their $w/(\text{CaO} + \text{MgO}_{\text{eq}} + \text{Na}_2\text{O}_{\text{eq}} + \text{K}_2\text{O}_{\text{eq}})$, together with data compiled for the previous analysis, is shown in Fig. 8. A relationship between $k_{\text{c-nat}}$ and $w/(\text{CaO} + \text{MgO}_{\text{eq}} + \text{Na}_2\text{O}_{\text{eq}} + \text{K}_2\text{O}_{\text{eq}})$ is evident, supporting the conclusions of the previous analysis and the usefulness of the $w/(\text{CaO} + \text{MgO}_{\text{eq}} + \text{Na}_2\text{O}_{\text{eq}} + \text{K}_2\text{O}_{\text{eq}})$ of AAMs to predict their carbonation resistance.

Despite the generally good correlation when considering the *full* range of AAM compositions, the coefficients of carbonation of AAMs with *similar* $w/(\text{CaO} + \text{MgO}_{\text{eq}} + \text{Na}_2\text{O}_{\text{eq}} + \text{K}_2\text{O}_{\text{eq}})$ can deviate

Table 4 Coefficients of carbonation (k_c in mm/ \sqrt{d}) of the concretes under natural (0.04 % CO₂) and accelerated (1 % CO₂ and 4 % CO₂) conditions.

CO ₂ concentration	C100	C80S20	C60S40	C40S60	C20S80	S100	CEM I
Natural (0.04 %)	1.59	1.05	0.55	0.29	0.58	0.46	0.21
1 %	2.50	4.16	2.40	0.92	2.40	2.11	0.61
4 %	6.73	6.37	5.96	1.03	7.16	4.87	0.68

^b Value uncertain. (Decision where to draw tangents was equivocal.)

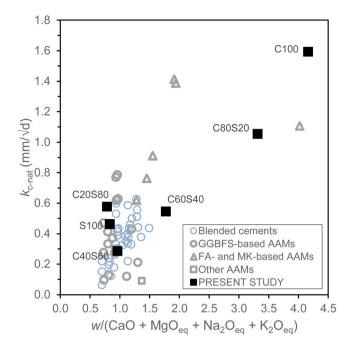


Fig. 8. Coefficients of carbonation obtained under natural carbonation conditions versus w/(CaO + MgO_{eq} + Na_2O_{eq} + K_2O_{eq}) ratios for the concretes in the present study, and for concretes and mortars analyzed in a previous study [13]. The data points from the present study are labelled with their respective concrete designations. In the previous analysis, 'GGBFS-based AAMs' denotes alkali-activated concretes and mortars with ≥ 50 % GGBFS in the binder, and 'FA- and MK-based AAMs' denotes alkali-activated concretes and mortars with > 50% fly ash or metakaolin in the binder; 'Blended cements' denotes concretes and mortars based on blended cements with ≥ 66 % (mostly ≥ 70 %) SCMs in the binder.

significantly from each other, as demonstrated here by S100, C20S80 and C40S60. Within this group, k_{c-nat} was lowest for C40S60, intermediate for S100, and highest for C20S80. However, XRD and TGA did not indicate substantial differences between the phase assemblages of these materials after curing as well as after natural carbonation, though DTG showed that the amount of carbonates after carbonation was higher for S100 than for the other two materials. Nevertheless, the pore structure of the three materials, as determined by MIP, differed considerably: C40S60 exhibited the smallest threshold radius and MIP porosity; the threshold radius of S100 was similar to that of C40S60, but the MIP porosity of S100 was considerably higher; and the threshold radius and MIP porosity of C20S80 were the highest among the three materials. Since MIP measures pore-entry size distributions, the obtained data is particularly relevant to degradation phenomena that are controlled to a large extent by transport processes [16,45], such as the carbonation of concrete. It is concluded that the low threshold radius and MIP porosity of C40S60 indicate a particularly dense (i.e., difficult-to-permeate) pore system, which led to its low k_{c-nat} . It can be generalized that the pore structure of AAMs is an important factor influencing their carbonation resistance and being responsible for a significant fraction of any deviation from the typical relation between k_{c-nat} and $w/(CaO + MgO_{eq} +$ $Na_2O_{eq}+K_2O_{eq}$). Thus, the influence of factors such as the reactivity of the starting materials, particle size distribution of the solid binder materials, composition of the activator solution etc. on the pore structure of AAMs, needs to be understood in more detail to improve our ability to predict the carbonation resistance of these materials.

4.2. Effect of CO2 concentration

If carbonation was completely diffusion-controlled, *i.e.*, if the square-root-of-time law [41,42] was followed at all CO₂ concentrations, the

ratio between the coefficients of carbonation obtained at two different CO_2 concentrations, all other conditions being equal, could be calculated according to [46,47]

$$\frac{k_{\text{c-acc}}}{k_{\text{c-nat}}} = \sqrt{\frac{c_{\text{CO2-acc}}}{c_{\text{CO2-nat}}}} \tag{1}$$

where $k_{\text{c-acc}}$ is the coefficient of carbonation obtained in accelerated carbonation testing, *i.e.*, at some CO₂ concentration higher than the natural concentration; $k_{\text{c-nat}}$ is the coefficient of carbonation obtained at natural CO₂ concentration; $c_{\text{CO2-acc}}$ is the CO₂ concentration employed for accelerated carbonation testing; and $c_{\text{CO2-nat}}$ is the natural CO₂ concentration in air (0.04 %). However, recent reviews have shown that for blended cement concretes [41] and particularly for AAMs [13] the coefficients of carbonation obtained under accelerated conditions tend to be lower than what is predicted by Eq. (1), although for AAMs the previously available data was scant.

Fig. 9 shows the coefficients of carbonation at natural CO₂ concentration, predicted from the measurements under accelerated conditions and application of Eq. (1), as a function of the measured coefficients of carbonation at natural CO₂ concentration for the alkali-activated concretes of the present study. For concretes C100 and C80S20, i.e., at $k_{\text{c-nat}} > 1 \text{ mm}/\sqrt{\text{d}}$, the predicted coefficients are considerably lower than the measured coefficients, both for accelerated testing at 1 % CO₂ and at 4 % CO₂. The deviation from Eq. (1) can also be demonstrated by plotting the measured $k_{\text{c-acc}}$ versus the measured $k_{\text{c-nat}}$ and comparing the data with the relationships predicted by Eq. (1); see Fig. S10. These findings confirm the conclusion of the previous analysis [13] that accelerated carbonation testing of low-Ca AAMs yields coefficients of carbonation that are lower than predicted by Eq. (1), i.e., coefficients that cannot be used to predict natural carbonation resistance by using that equation.

Contrary to the inferences of the earlier analysis, the present study shows that accelerated testing cannot even be used to reliably rank the carbonation resistance of low-Ca AAMs, as demonstrated by the fact that $k_{\text{c-nat}}$ was lower for C80S20 than for C100, as expected, while the order of their $k_{\text{c-acc}}$ obtained at 1 % CO₂ was reversed (Table 2, Fig. 9). This

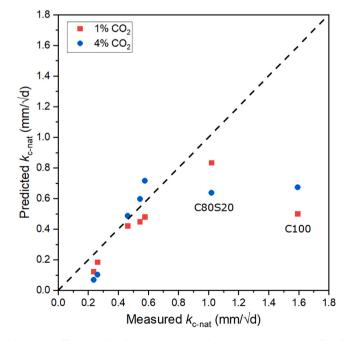


Fig. 9. Coefficients of carbonation at natural ${\rm CO_2}$ concentration, predicted from the measurements under accelerated conditions and application of Eq. (1), versus measured coefficients of carbonation at natural ${\rm CO_2}$ concentration. The dashed line is the line of equality.

might be an extreme case, and the reversal of the order of performances is likely not always observed; however, the present observations demonstrate that the uncritical use of accelerated carbonation testing of low-Ca AAMs can be misleading. In any case, the fact that no simple (linear) relationship exists between the $k_{\text{C-acc}}$ and the $k_{\text{c-nat}}$ of AAMs means that the relationship between carbonation resistance and $w/(\text{CaO} + \text{MgO}_{\text{eq}} + \text{Na}_2\text{O}_{\text{eq}} + \text{K}_2\text{O}_{\text{eq}})$ is not observed in accelerated carbonation testing (Fig. S11), making accelerated testing less suitable to examine the influence of AAM composition on their properties.

Although the present results provide strong support for a deviation from purely diffusion-controlled carbonation rate for low-Ca AAMs at higher-than-natural CO2 concentrations, elucidation of the underlying mechanisms is difficult. Previous work [48] has indicated that, generally, C-(N-)A-S-H is a major binding phase in AAMs with a GGBFS fraction of more than ~25 %, while N-A-S-H is predominant or the only binding phase at lower GGBFS fractions (the balance being a reactive aluminosilicate starting material). Thus, a major difference between concretes C100 and C80S20 on the one hand and the materials with a higher fraction of GGBFS on the other hand is presumably the predominance of N-A-S-H in the former and the presence of a significant amount of C-(N-)A-S-H in the latter. Further, due to the high Na concentrations and low Ca fractions in C100 and C80S20, their carbonation products differed from those of the other materials: A substantial amount of nahcolite was identified by XRD in C100 and C80S20 after accelerated carbonation (1 % and 4 % CO2), while the amount of this phase was either very low (C60S40, C40S60, C20S80) or it was not present (S100) in the other AAMs. It is conceivable that these characteristics are associated with changes of the diffusion coefficient of CO2 and/or altered carbonation reaction kinetics; however, whether a causal relationship really exists between these characteristics and the deviating carbonation rate behavior of low-Ca AAMs cannot be answered based solely on the present data.

5. Summary and conclusions

Concretes based on alkali-activated GGBFS/CC blends with systematically varied fractions of GGBFS and CC require optimization, leading to varied activator solution contents and compositions, to yield both acceptable workability in the fresh state and sufficient mechanical strength after curing, *i.e.*, to obtain concretes that can be considered as being representative of materials that can be applied for construction purposes. Despite the variation of some of the mix-design parameters, the composition of the paste fractions of these concretes can be approximately described by a single parameter, the $w/(\text{CaO} + \text{MgO}_{\text{eq}} + \text{Na}_2\text{O}_{\text{eq}})$ ratio, as far as carbonation resistance is concerned.

The coefficient of carbonation of the concretes at natural CO2 concentration, k_{c-nat} , exhibits a reasonable correlation with this ratio over a wide compositional range, i.e., spanning all compositions from 100 % GGBFS to 100 % CC. This can be explained by the fact that the porosity of AAMs depends on their water content, while alkali metals and alkaline-earth metals in their reaction products are able to bind CO₂ as carbonates. However, for concretes with similar w/(CaO + MgO_{eq} + $Na_2O_{eq} + K_2O_{eq}$) ratios, significant differences between their k_{c-nat} can still be observed. The present results indicate that these differences are caused by differences between their pore structures, which can be approximately represented as the threshold radius determined by MIP. Concrete C40S60 with $w/(CaO + MgO_{eq} + Na_2O_{eq} + K_2O_{eq}) = 0.96$ and a particularly low threshold radius, exhibited a k_{c-nat} which was comparable to that of a Portland cement concrete tested as a reference. Thus, the $w/(CaO + MgO_{eq} + Na_2O_{eq} + K_2O_{eq})$ ratio is a suitable parameter to obtain an approximate estimate of the carbonation resistance of an AAM, while a more accurate prediction will require a better understanding of the parameters that determine the pore structure of AAMs as they relate to transport processes, i.e., pore-entry size distribution, pore size distribution and pore connectivity. It is anticipated that this is particularly important if the influence of relative humidity on

carbonation rate is to be considered.

Accelerated carbonation testing of low-Ca AAMs, *i.e.*, the concretes with 100 % or 80 % CC in the binder, at a CO $_2$ concentration of 1 % or 4 % yielded coefficients of carbonation that were considerably lower than what is expected from application of the square-root-of-time law. Importantly, this means that results from accelerated testing cannot be used to predict the carbonation resistance of low-Ca AAMs under natural conditions until suitable relationships for this conversion have been developed. In addition, the relationship between the coefficients of carbonation and $w/(\text{CaO} + \text{MgO}_{eq} + \text{Na}_2\text{O}_{eq} + \text{K}_2\text{O}_{eq})$, which is observed for carbonation at natural CO $_2$ concentration, does not emerge in accelerated carbonation testing, making accelerated testing less suitable for studying the carbonation resistance of AAMs. Resolution of these issues will require an improved understanding of the mechanisms that underlie the observed carbonation behavior at higher-than-natural CO $_2$ concentrations.

CRediT authorship contribution statement

Luís U.D. Tambara Jr.: Writing – original draft, Visualization, Methodology, Investigation, Formal analysis. **Astrid Hirsch:** Writing – review & editing, Investigation. **Frank Dehn:** Writing – review & editing, Methodology, Funding acquisition, Conceptualization. **Gregor J.G. Gluth:** Writing – review & editing, Supervision, Methodology, Funding acquisition, Formal analysis, Conceptualization.

Declaration of Competing Interest

The authors declare that they have no known competing financial interests or personal relationships that could have appeared to influence the work reported in this paper.

Data Availability

Data will be made available on request.

Acknowledgements

The work leading to the present results was funded by the *Deutsche Forschungsgemeinschaft* (DFG, German Research Foundation) – Project number 492587490, which is gratefully acknowledged.

Appendix A. Supporting information

Supplementary data associated with this article can be found in the online version at doi:10.1016/j.conbuildmat.2024.138351.

References

- [1] J.L. Provis, Alkali-activated materials, Cem. Concr. Res. 114 (2018) 40–48, https://doi.org/10.1016/j.cemconres.2017.02.009.
- [2] G. Habert, S.A. Miller, V.M. John, J.L. Provis, A. Favier, A. Horvath, K.L. Scrivener, Environmental impacts and decarbonization strategies in the cement and concrete industries, Nat. Rev. Earth Environ. 1 (2020) 559–573, https://doi.org/10.1038/ s43017-020-0093-3.
- [3] G. Gluth, C. Grengg, N. Ukrainczyk, F. Mittermayr, M. Dietzel, Acid resistance of alkali-activated materials: recent advances and research needs, RILEM Tech. Lett. 7 (2022) 58–67. https://doi.org/10.21809/rilemtechlett.2022.157.
- [4] S.A. Bernal, J.L. Provis, D.G. Brice, A. Kilcullen, P. Duxson, J.S.J. Van Deventer, Accelerated carbonation testing of alkali-activated binders significantly underestimates service life: The role of pore solution chemistry, Cem. Concr. Res. 42 (2012) 1317–1326. https://doi.org/10.1016/j.cemconres.2012.07.002.
- [5] M. Babaee, M.S.H. Khan, A. Castel, Passivity of embedded reinforcement in carbonated low-calcium fly ash-based geopolymer concrete, Cem. Concr. Compos. 85 (2018) 32–43, https://doi.org/10.1016/j.cemconcomp.2017.10.001.
- [6] S.A. Bernal, R.M. de Gutierrez, J.L. Provis, V. Rose, Effect of silicate modulus and metakaolin incorporation on the carbonation of alkali silicate-activated slags, Cem. Concr. Res. 40 (2010) 898–907, https://doi.org/10.1016/j. cemconres.2010.02.003.

- [7] F. Puertas, M. Palacios, T. Vázquez, Carbonation process of alkali-activated slag mortars, J. Mater. Sci. 41 (2005) 3071–3082, https://doi.org/10.1007/s10853-005.1821-2
- [8] M. Palacios, F. Puertas, Effect of carbonation on alkali-activated slag paste, J. Am. Ceram. Soc. 89 (2006) 3211–3221, https://doi.org/10.1111/j.1551-2916.2006.01214.x.
- [9] S.D.C. Gomes, Q.D. Nguyen, W. Li, A. Castel, Carbonation resistance of calcined clay-ground granulated blast furnace slag alkali-activated mortar, Constr. Build. Mater. 393 (2023) 131811, https://doi.org/10.1016/j.conbuildmat.2023.131811.
- [10] R. Pouhet, M. Cyr, Formulation and performance of flash metakaolin geopolymer concretes, Constr. Build. Mater. 120 (2016) 150–160, https://doi.org/10.1016/j. conbuildmat.2016.05.061.
- [11] J.L. Provis, K. Arbi, S.A. Bernal, D. Bondar, A. Buchwald, A. Castel, S. Chithiraputhiran, M. Cyr, A. Dehghan, K. Dombrowski-Daube, A. Dubey, V. Ducman, G.J.G. Gluth, S. Nanukuttan, K. Peterson, F. Puertas, A. van Riessen, M. Torres-Carrasco, G. Ye, Y. Zuo, RILEM TC 247-DTA round robin test: mix design and reproducibility of compressive strength of alkali-activated concretes, Mater. Struct. 52 (2019) 99, https://doi.org/10.1617/s11527-019-1396-z.
- [12] G.J.G. Gluth, K. Arbi, S.A. Bernal, D. Bondar, A. Castel, S. Chithiraputhiran, A. Dehghan, K. Dombrowski-Daube, A. Dubey, V. Ducman, K. Peterson, P. Pipilikaki, S.L.A. Valcke, G. Ye, Y. Zuo, J.L. Provis, RILEM TC 247-DTA round robin test: carbonation and chloride penetration testing of alkali-activated concretes, Mater. Struct. 53 (2020) 21, https://doi.org/10.1617/s11527-020-1449-3.
- [13] G.J.G. Gluth, X. Ke, A. Vollpracht, L. Weiler, S.A. Bernal, M. Cyr, K. Dombrowski-Daube, D.A. Geddes, C. Grengg, C. Le Galliard, M. Nedeljkovic, J.L. Provis, L. Valentini, B. Walkley, Carbonation rate of alkali-activated concretes and high-volume SCM concretes: a literature data analysis by RILEM TC 281-CCC, Mater. Struct. 55 (2022) 225, https://doi.org/10.1617/s11527-022-02041-4.
- [14] N.S. Msinjili, G.J.G. Gluth, P. Sturm, N. Vogler, H.-C. Kühne, Comparison of calcined illitic clays (brick clays) and low-grade kaolinitic clays as supplementary cementitious materials, Mater. Struct. 52 (2019) 94, https://doi.org/10.1617/ s11527-019-1393-2.
- [15] N.S. Msinjili, N. Vogler, P. Sturm, M. Neubert, H.-J. Schröder, H.-C. Kühne, K.-J. Hünger, G.J.G. Gluth, Calcined brick clays and mixed clays as supplementary cementitious materials: effects on the performance of blended cement mortars, Constr. Build. Mater. 266 (2021) 120990, https://doi.org/10.1016/j.conbuildmat.2020.120990.
- [16] S. Diamond, Mercury porosimetry: an inappropriate method for the measurement of pore size distributions in cement-based materials, Cem. Concr. Res. 30 (2000) 1517–1525, https://doi.org/10.1016/S0008-8846(00)00370-7.
- [17] D.N. Winslow, S. Diamon, A mercury porosimetry study of the evolution of porosity in Portland cement, J. Mater. 5 (1970) 564–585.
- [18] S.A. Bernal, R. San Nicolas, R.J. Myers, R. Mejía De Gutiérrez, F. Puertas, J.S.J. Van Deventer, J.L. Provis, MgO content of slag controls phase evolution and structural changes induced by accelerated carbonation in alkali-activated binders, Cem. Concr. Res. 57 (2014) 33–43, https://doi.org/10.1016/j.cemconres.2013.12.003.
- [19] Z. Liu, P. Van den Heede, C. Zhang, X. Shi, L. Wang, J. Li, Y. Yao, B. Lothenbach, N. De Belie, Carbonation of blast furnace slag concrete at different CO₂ concentrations: carbonation rate, phase assemblage, microstructure and thermodynamic modelling, Cem. Concr. Res. 169 (2023) 107161, https://doi.org/ 10.1016/j.cemconres.2023.107161.
- [20] E.M. Barral, L.B. Rogers, Differential thermal analysis of the decomposition of sodium bicarbonate and its simple double salts, J. Inorg. Nucl. Chem. 28 (1966) 41–51, https://doi.org/10.1016/0022-1902(66)80226-9.
- [21] B. Lothenbach, P. Durdziński, K.D. Weerdt, Thermogravimetric analysis, in: K. Scrivener, R. Snellings, B. Lothenbach (Eds.), A Practical Guide to Microstructural Analysis of Cementitious Materials, CRC Press, Boca Raton, 2016, pp. 177–211.
- [22] M. Thiery, G. Villain, P. Dangla, G. Platret, Investigation of the carbonation front shape on cementitious materials: effects of the chemical kinetics, Cem. Concr. Res. 37 (2007) 1047–1058, https://doi.org/10.1016/j.cemconres.2007.04.002.
- [23] R.V. Siriwardane, J.A. Poston, C. Robinson, T. Simonyi, Effect of additives on decomposition of sodium carbonate: precombustion CO₂ capture sorbent regeneration, Energy Fuels 25 (2011) 1284–1293, https://doi.org/10.1021/ ef101486m.
- [24] T. Stanimirova, N. Piperov, N. Petrova, G. Kirov, Thermal evolution of Mg-Al-CO₃ hydrotalcites, Clay Min. 39 (2004) 177–191, https://doi.org/10.1180/ 0009855043920129.
- [25] B. Lafuente, R.T. Downs, H. Yang, N. Stone, The power of databases: the RRUFF project, in: T. Armbruster, R.M. Danisi (Eds.), Highlights in Mineralogical Crystallography, De Grutyer, Berlin, 2015, pp. 1–29.
- [26] O. Rudić, F. Mittermayr, G.J.G. Gluth, S. Simon, N. Ukrainczyk, Y. Seyrek, B. Freytag, J. Juhart, C. Grengg, On the benefits of vegetable oil addition for the pore structure and acid resistance of alkali-activated systems, Ceram. Int. 49 (2023) 33275–33290, https://doi.org/10.1016/j.ceramint.2023.08.036.
- [27] X. Ke, S.A. Bernal, T. Sato, J.L. Provis, Alkali aluminosilicate geopolymers as binders to encapsulate strontium-selective titanate ion-exchangers, Dalton Trans. 48 (2019) 12116–12126, https://doi.org/10.1039/c9dt02108f.

- [28] L. Black, Raman spectroscopy of cementitious materials, in: J. Yarwood, R. Douthwaite, S. Duckett (Eds.), Spectroscopic Properties of Inorganic and Organometallic Compounds Vol. 40, Royal Society of Chemistry, 2009, pp. 72–127, https://doi.org/10.1039/b715000h.
- [29] R.J. Kirkpatrick, J.L. Yarger, P.F. McMillan, P.C. Yu, X. Cong, Raman spectroscopy of C-S-H, tobermorite, and jennite, Adv. Cem. Based Mater. 5 (1997) 93–99, https://doi.org/10.1016/S1065-7355(97)00001-1.
- [30] S. Ortaboy, J. Li, G. Geng, R.J. Myers, P.J.M. Monteiro, R. Maboudian, C. Carraro, Effects of CO₂ and temperature on the structure and chemistry of C-(A-)S-H investigated by Raman spectroscopy, RSC Adv. 7 (2017) 48925–48933, https:// doi.org/10.1039/c7ra07266i.
- [31] S. Martinez-Ramirez, S. Sanchez-Cortes, J.V. Garcia-Ramos, C. Domingo, C. Fortes, M.T. Blanco-Varela, Micro-Raman spectroscopy applied to depth profiles of carbonates formed in lime mortar, Cem. Concr. Res. 33 (2003) 2063–2068, https://doi.org/10.1016/s0008-8846(03)00227-8.
- [32] S. Shagñay, A. Bautista, F. Velasco, M. Torres-Carrasco, Carbonation of alkaliactivated and hybrid mortars manufactured from slag: confocal Raman microscopy study and impact on wear performance, Bol. Soc. Esp. Cerám. Vidr. 62 (2023) 428–442. https://doi.org/10.1016/j.bsecv.2022.07.003.
- [33] U. Wehrmeister, A.L. Soldati, D.E. Jacob, T. Häger, W. Hofmeister, Raman spectroscopy of synthetic, geological and biological vaterite: a Raman spectroscopic study, J. Raman Spectrosc. 41 (2009) 193–201, https://doi.org/ 10.1002/jrs.2438.
- [34] M. Torres-Carrasco, A. del Campo, M.A. de la Rubia, E. Reyes, A. Moragues, J. F. Fernández, New insights in weathering analysis of anhydrous cements by using high spectral and spatial resolution Confocal Raman Microscopy, Cem. Concr. Res. 100 (2017) 119–128, https://doi.org/10.1016/j.cemconres.2017.06.003.
- [35] D. Chakrabarty, S. Mahapatra, Aragonite crystals with unconventional morphologies, J. Mater. Chem. 9 (1999) 2953–2957, https://doi.org/10.1039/ A005407C
- [36] P. Vargas Jentzsch, V. Ciobota, P. Rosch, J. Popp, Reactions of alkaline minerals in the atmosphere, Angew. Chem. Int. Ed. Engl. 52 (2013) 1410–1413, https://doi. org/10.1002/anje.201208319.
- [37] M. Getenet, J.M. Garcia-Ruiz, F. Otalora, F. Emmerling, D. Al-Sabbagh, C. Verdugo-Escamilla, A comprehensive methodology for monitoring evaporitic mineral precipitation and hydrochemical evolution of saline lakes: the case of Lake Magadi soda brine (East African Rift Valley, Kenya), Cryst. Growth Des. 22 (2022) 2307–2317, https://doi.org/10.1021/acs.cgd.1c01391.
- [38] P. Vargas Jentzsch, B. Kampe, V. Ciobota, P. Rosch, J. Popp, Inorganic salts in atmospheric particulate matter: Raman spectroscopy as an analytical tool, Spectrochim. Acta A 115 (2013) 697–708, https://doi.org/10.1016/j. saa.2013.06.085.
- [39] A. Bertoluzza, P. Monti, M.A. Morelli, M.A. Battaglia, A Raman and infrared spectroscopic study of compounds characterized by strong hydrogen bonds, J. Mol. Struct. 73 (1981) 19–29, https://doi.org/10.1016/0022-2860(81)85042-9.
- [40] S.A. Bernal, J.L. Provis, B. Walkley, R. San Nicolas, J.D. Gehman, D.G. Brice, A. R. Kilcullen, P. Duxson, J.S.J. Van Deventer, Gel nanostructure in alkali-activated binders based on slag and fly ash, and effects of accelerated carbonation, Cem. Concr. Res. 53 (2013) 127–144, https://doi.org/10.1016/j.cem.concres 2013 06 007
- [41] S. von Greve-Dierfeld, B. Lothenbach, A. Vollpracht, B. Wu, B. Huet, C. Andrade, C. Medina, C. Thiel, E. Gruyaert, H. Vanoutrive, I.F. Saéz del Bosque, I. Ignjatovic, J. Elsen, J.L. Provis, K. Scrivener, K.-C. Thienel, K. Sideris, M. Zajac, N. Alderete, Ö. Cizer, P. Van den Heede, R.D. Hooton, S. Kamali-Bernard, S.A. Bernal, Z. Zhao, Z. Shi, N. De Belie, Understanding the carbonation of concrete with supplementary cementitious materials: a critical review by RILEM TC 281-CCC, Mater. Struct. 53 (2020) 136, https://doi.org/10.1617/s11527-020-01558-w.
- [42] C.L. Page, K.W.J. Treadaway, Aspects of the electrochemistry of steel in concrete, Nature 297 (1982) 109–115, https://doi.org/10.1038/297109a0.
- [43] A. Leemann, P. Nygaard, J. Kaufmann, R. Loser, Relation between carbonation resistance, mix design and exposure of mortar and concrete, Cem. Concr. Compos. 62 (2015) 33–43, https://doi.org/10.1016/j.cemconcomp.2015.04.020.
- [44] A. Leemann, F. Moro, Carbonation of concrete: the role of CO₂ concentration, relative humidity and CO₂ buffer capacity, Mater. Struct. 50 (2017) 30, https://doi.org/10.1617/s11527-016-0917-2.
- [45] R.F. Feldman, Pore structure, permeability and diffusivity as related to durability, in: 8th International Congress on the Chemistry of Cement, Rio de Janeiro, Brazil, 1986, Vol. 1, pp. 336-356.
- [46] V.G. Papadakis, C.G. Vayenas, M.N. Fardis, Fundamental modeling and experimental investigation of concrete carbonation, ACI Mater. J. 88 (1991) 363–373, https://doi.org/10.14359/1863.
- [47] K. Sisomphon, L. Franke, Carbonation rates of concretes containing high volume of pozzolanic materials, Cem. Concr. Res. 37 (2007) 1647–1653, https://doi.org/ 10.1016/j.cemconres.2007.08.014.
- [48] I. Ismail, S.A. Bernal, J.L. Provis, R. San Nicolas, S. Hamdan, J.S.J. Van Deventer, Modification of phase evolution in alkali-activated blast furnace slag by the incorporation of fly ash, Cem. Concr. Compos. 45 (2014) 125–135, https://doi. org/10.1016/j.cemconcomp.2013.09.006.